Supplementary Materials

Computational modelling of cerebrospinal fluid flow in a translational canine model

Ryan Jones[1], Clare Rusbridge[1,2], Srdjan Cirovic[3]

[1]The School of Veterinary Medicine, University of Surrey, Guildford GU2 7AL, UK.
[2]Wear Referrals Veterinary Specialist & Emergency Hospital, Stockton-on-Tees TS21 2ES, UK.
[3]School of Engineering, University of Surrey, Guildford GU2 7XH, UK.

Correspondence to: Ryan Jones, The School of Veterinary Medicine, University of Surrey, Guildford GU2 7AL, UK. E-mail: rj00642@surrey.ac.uk

ORCID: Ryan Jones (0009-0009-3226-3386), Clare Rusbridge (0000-0002-3366-2110), Srdjan Cirovic (0000-0003-3284-2897)

1. SIMULATION SETUP

1.1 Geometric Reconstruction

3D reconstruction of ventricular system, cranial and spinal subarachnoid spaces, and central canal was performed by a single operator (author R.J.). All images used in this study were acquired using a 1.5 T MRI protocol described by Rusbridge *et al.,* 2018[1].

Table A. Diagnostic imaging protocols used in this study, detailed by Rusbridge *et al.*, 2018[1]

	T2 Sagittal Brain	**T2 Transverse Brain**	**MPRAGE Dorsal Brain**	**T2 Sagittal Spine**
Field of View [mm]	170 × 170	140 × 98	180 × 135	260 × 260
Slice Thickness [mm]	2.7	3.5	0.7	1.5
Slice Gap [%]	20	10	50	10
Repetition Time [ms]	2380	3470	2200	3990
Echo Time [ms]	99	95	3.48	105

Flip Angle [deg]	150	150	8	180
Image Matrix	266 × 320	186 × 320	192 × 256	358 × 448
Bandwidth [Hz/Px]	80	65	150	151
Scan Time [min:sec]	4:35	4:08	5:07	5:09

T2-weighted sagittal images of the brain were interpolated using B-spline interpolation onto a 0.2 mm isotropic grid in 3D Slicer (version 5.8.0). Transverse T2-weighted sequences were resampled onto the same grid and combined to form a composite volume. The ventricular system was segmented directly from the interpolated MRI due to its sufficient cross-sectional thickness relative to voxel size. In contrast, the cranial SAS in brachycephalic dogs was frequently below single voxel resolution, appearing as a single-pixel layer in raw images. To approximate this structure, the brain parenchyma was segmented, smoothed using Gaussian filtering, hollowed, and uniformly dilated outward by a thickness equal to the in-plane pixel size (~0.4 mm) to generate a physiologically consistent SAS envelope. Larger cisternal regions, the quadrigeminal and interpeduncular cisterns and cisterna magna, were segmented directly and merged into the SAS geometry using Boolean union operations.

Models of the spinal SAS from the rostral margin of C1 to the T3/4 disc were readily available for this data from a previous study[2]. These models were generated by drawing contours of the SAS at specific anatomically significant locations, which were used within this study as datums upon which data were collected. The central canal was reconstructed by fitting a spline to the central canal centerline in 3D Slicer identified from MRI, and sweeping a cylindrical profile of diameter of a single voxel in the raw MRI data (~0.4 mm) along this path.

Surface models of all CSF compartments were exported to MeshLab (ISTI-CNR, Italy) for explicit isotropic remeshing to improve element uniformity. Re-meshed surfaces were then imported into Blender (4.5, Blender Foundation, Amsterdam, Netherlands) for manual refinement, including artifact removal and surface bridging to ensure continuity. Final geometries were re-imported into ANSYS SpaceClaim (2024 R2, ANSYS Inc., Canonsburg, PA, USA) and converted to solid bodies for volume meshing.

For each of the 9 resulting models, a polyhedral volume mesh was generated in ANSYS Fluent (2024 R2, ANSYS Inc., Canonsburg, PA, USA) with 5 layers of prismatic boundary layer cells applied at the walls to better resolve near-wall flows. Table B provides the final mesh cell counts.

Table B. Mesh count, peak inlet flowrate, and effective compliance for each of the 9 subjects considered suitable for computational modelling

	Mesh Cell Count (× 10^6)	**Inlet Peak Flowrate [ml/min]**	**Effective Compliance [µl/Pa]**
1	1.49	23.11	0.29
2	1.60	26.79	0.34
3	3.34	22.23	0.28
4	1.54	28.44	0.36
5	1.35	26.48	0.34
6	1.45	19.32	0.25
7	0.97	26.11	0.33
8	5.03	26.08	0.33
9	1.37	22.60	0.29

1.2. Boundary Conditions and Physiological Assumptions

Time-varying velocity and pressure conditions were prescribed to reproduce CSF motion over the cardiac cycle (Fig. 2). These conditions were implemented using user-defined functions within ANSYS Fluent. A no-slip condition was applied to all remaining boundaries, meaning that there was no relative motion between fluid in contact with the walls, and the walls themselves.

Arterial expansion during systole increases brain volume, displacing the neural tissue and forcing CSF toward the spinal SAS where compliance is higher. As the amplitude of the displacement of neural tissue is very small (in the order of micrometers), this was implemented via a velocity boundary condition rather than a moving-wall boundary, as per Fillingham *et al.,* 2022, capturing the resulting CSF motion while avoiding the computational expense of deforming boundaries[3]. Displacement was assumed to occur homogeneously across the ventricular system and the internal surface of the cranial SAS, consistent with the small magnitude and diffuse nature of cardiac-driven parenchymal motion.

A periodic inlet waveform was defined based on experimental CSF flow data presented by Rich *et al.,* 2024 to satisfy physiological constraints: smooth continuity, zero net volumetric flow over one cardiac cycle, caudal systolic dominance, and temporal asymmetry with peak caudal flow at ~10% and peak rostral flow at ~80% of the cycle[4]. A nested sinusoid was selected as a compact analytic representation requiring fewer harmonic components than a truncated Fourier series (Equ. [A]).

$$Q(t) = A\sin(\sin((2\pi ft + \psi) + 2\pi ft)) + C \qquad [A]$$

The cardiac frequency was set to f=1.37 Hz (82.4 bpm[5]) as a representative heart rate for CKCS. Parameters A=0.15 and C=0.05 were selected to encode the required systolic–diastolic asymmetry. The phase shift ψ was solved by minimizing $J(\psi) = \left|\int_0^T Q(t;\psi)dt\right|$ to enforce zero net flux over a cardiac cycle (T), yielding ψ =-0.8582 rad.

In a prior investigation, the velocity at the inlet boundary for a single model was determined by using an iterative approach, the waveform amplitude was scaled to produce peak aqueduct systolic velocity of 0.72 cm/s reported in dogs of comparable weight[4]. This yielded a peak inlet flowrate of 26.79 ml/min, and the resulting simulations provided good agreement with literature. There is evidence that the relationship between cerebral blood flowrate and brain volume is approximately linear in mammals[6]. Therefore, the peak flowrates of the waveforms for each participant were scaled using their brain volume, shown in Table B. The inlet velocity was applied over the ventricular surface and inner cranial SAS boundary to achieve the desired aqueduct velocity.

Cranially, the rigid skull constrains volumetric expansion, resulting in negligible compliance and minimal energy storage. In contrast, the spinal dura mater exhibits measurable compliance and acts as a reservoir, storing and releasing energy over the cardiac cycle and thereby modulating pressure gradients. In the computational models this was represented by a single lumped linear compliance at the caudal end. Pressure at the caudal end was determined as Eq. [B].

$$P(t) = \frac{1}{C}\int_0^t Q(t')\,dt' \qquad [B]$$

Where constant compliance C was derived from canine intrathecal pressure recordings reported by Novak *et al., 1974* demonstrating a mean pressure gradient of 152 Pa over the

cardiac cycle[7]. This approach implicitly mimics the compliance of the spinal dura mater without requiring computationally expensive moving-wall or fluid–structure interaction simulation. The effective compliances of each model are presented in Table B.

1.3 Numerical Setup

All simulations were performed in ANSYS Fluent. An unsteady laminar solver was employed with a timestep of dt=T/80, where T=1/f. Simulations were advanced for three cardiac cycles, and results from the final cycle were used for analysis to ensure periodic convergence. CSF was modelled as a Newtonian fluid, with dynamic viscosity (μ=0.001003 Pa·s) and density (ρ=998.2 kg/m^3) of water. The movement of CSF was governed by the Navier-Stokes equation and mass continuity for an incompressible fluid Eq. [C] and [D].

$$\nabla \cdot \mathbf{u} = 0 \qquad [C]$$

$$\rho \frac{D\mathbf{u}}{Dt} = -\nabla p + \boldsymbol{\mu} \nabla^2 \mathbf{u} \qquad [D]$$

Pressure–velocity coupling was resolved using the SIMPLEC algorithm with a skewness correction factor of 2 to maintain numerical stability. A maximum of 70 iterations per timestep was allowed to ensure convergence within each step. Transverse planes orthogonal to the sagittal plane were defined along the craniospinal axis at the rostral margin of C1, insertion of the apical ligament, dorsal aspect of the dens, dens-axis junction, and mid-point of each vertebral body and disc between C2 and the T3/4 disc to collect quantitative flow data. Post-processing and data analysis were performed in MATLAB (MathWorks, Natick, MA, USA), while qualitative flow visualization and field inspection were conducted in CFD-Post (ANSYS Inc., Canonsburg, PA, USA).

2. SENSITIVITY STUDIES

A series of independence studies were conducted on a representative model as part of a prior study. This model was generated from a model included in the present study, with the notable distinction that the spine extended down to the second lumbar vertebrae. The models presented in this study therefore represent a truncated version of this geometry.

2.1 Mesh-Independence

A mesh independence study ensures that the results of the simulation are independent of mesh size and quality. A steady simulation was initiated on four successively refined unstructured

polyhedral meshes of approximately 0.8M, 2.7M, 4.5M, and 8.1M cells (denoted very coarse, coarse, medium, and fine, respectively). The velocity inlet condition was applied to the inner surface of the SAS, and ventricular system, and a zero pressure condition was applied to the caudal end of the spine. Maximum velocity, flowrate, and pressure were monitored at two planes, one located at the foramen magnum and the other at C2. The CSF was modelled as a Newtonian fluid in a laminar flow regime, with the same properties as water. The simulation was run for 120 iterations.

Relative errors for each quantity ϕ were computed with respect to the fine mesh solution. All monitored quantities exhibited asymptotic grid convergence, with the medium mesh consistently providing relative errors of less than 2%. For mean pressure, and max velocity, the order of convergence p and the extrapolated "infinite resolution" solution ϕ_{ext} were estimated using Richardson extrapolation (Equ. E).

$$\phi_{ext} = \phi_3 + \frac{\phi_3 - \phi_2}{r^p - 1} \qquad (E)$$

Where r is the refinement ratio $r = h_2/h_3$, h are the mesh cell sizes, and the order of convergence $p = \frac{\ln\left(\frac{\phi_2 - \phi_1}{\phi_3 - \phi_2}\right)}{\ln r}$. This provides an estimate of the "true" solution in the limit of infinite mesh resolution, and allows assessment of how close the finest tested mesh is to the asymptotic value.

Table C. Mesh convergence and sensitivity analysis for peak CSF velocity and mean pressure

	Order of convergence, p	**Percentage Error $\left(1 - \frac{\phi_3}{\phi_{ext}}\right) \times 100$**	**Abs error $(\phi_{ext} - \phi_3)$**
Peak Velocity [cm/s]			
Foramen Magnum	2.20	0.45	5.8E-05
C2	2.18	0.32	6.4E-05
Mean Pressure [mPa]			
Foramen Magnum	0.28	8.77	0.04
C2	0.52	4.91	0.03

Table C presents the mesh sensitivity analysis for peak velocity and mean pressure at the foramen magnum and C2. The computational domain represents a highly complex geometry

which imposes practical bounds on admissible mesh resolutions. Below a certain cell count, mesh generation fails due to unacceptable element quality, while further refinement beyond the upper bound is precluded by computational cost. Consequently, only a finite window of mesh densities exists for which a valid mesh with acceptable quality metrics can be generated. Within this admissible range, velocity metrics exhibit clear convergence. Pressure metrics, by contrast, show slower and less regular convergence when assessed using a strict raw convergence criterion. However, the absolute differences in mean pressure between the finest mesh and the Richardson-extrapolated solution are very small, on the order of fractions of a millipascal.

The apparent lack of pressure convergence reflects the fact that pressure is already effectively converged at the coarsest viable mesh. Further coarsening is not practically possible, as it would fall outside the lower bound of the admissible mesh window and result in mesh failure. Thus, the pressure solution lies in a region of mesh parameter space that exceeds the practical convergence threshold but cannot be extended further in the coarse direction. Given that the primary objectives of this study concern cerebrospinal fluid kinematics and transport, which are governed predominantly by local velocity fields, mesh selection was based on velocity convergence. If absolute pressure values or strongly coupled fluid–structure interactions are of interest, additional mesh refinement or targeted pressure-focused mesh strategies would be required. The observed order of convergence for max velocity was approximately $p \sim 2.2$ which is consistent with the nominal second-order accuracy of the discretisation scheme. This suggests that the simulations are in the asymptotic grid convergence range, and that further refinement would decrease the discretisation error at a rate proportional to $h\hat{}2$. Thus, the fine mesh can be considered mesh independent for the purposes of this study.

Convergence was assessed using pressure histories at the inlet and cervical planes of the medium-mesh simulation. A tolerance of 10^{-4} mPa sustained over at least five consecutive iterations was used to exclude isolated fluctuations. Iteration-to-iteration pressure changes were evaluated against this criterion, and the first sustained occurrence was recorded. Using this approach, convergence was achieved by iteration 68 at the cervical planes and iteration 70 at the inlet.

2.2 Period-Independence

A period independence study ensures the periodic solution has settled, ensuring that the solution is periodically stable. An unsteady simulation was initiated using the transient velocity and pressure conditions presented in the materials and methods, this was run for 5 cardiac cycles at three timesteps corresponding to fractions of the cardiac cycle (dt = T/20, T/40, and T/80). The solver used was SIMPLEC, with a skewness correction factor of 2, which was found necessary to maintain solution stability. Skewness correction in accounts for non-orthogonality in the mesh, modifying the gradient interpolation to prevent numerical errors in regions of highly skewed cells. While this introduces a small amount of numerical diffusion, it is negligible for the laminar CSF flows considered here and ensures that the computed velocities and pressures are physically consistent and free from artefacts caused by the mesh.

Like the mesh sensitivity study, two planes were defined at C2 and the foramen magnum, upon which the flowrate, mean pressure, and max velocity were extracted. The root mean square error (RMSE) for each cycle was calculated relative to the previous cycle (Equ. F).

$$RMSE_i = \sqrt{\frac{1}{N}\sum_{j=1}^{N}\left(\phi_j^{(i)} - \phi_j^{(i-1)}\right)^2} \qquad (F)$$

Where N is the number of points per cycle, and $\phi_j^{(i)}$ is the value of the variable ϕ at point j in cycle i.

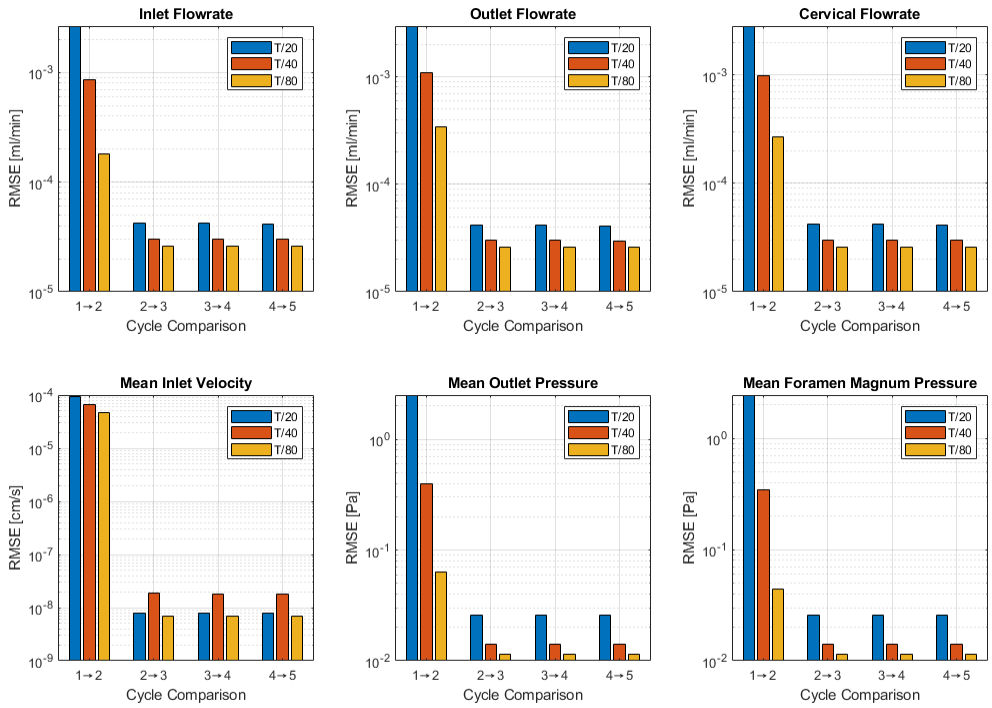

Figure A. Cycle-to-cycle root mean square error (RMSE) for key flow and pressure variables across successive cardiac cycles. RMSE is shown for inlet, outlet, and cervical flow rates, mean inlet velocity, mean outlet pressure, and mean foramen magnum pressure, comparing consecutive cycles (1–2 through 4–5). Shown on a logarithmic scale for three temporal resolutions.

Fig. A shows that the simulations rapidly reach a quasi-stead periodic state; the solution had effectively converged after the first cycle, and subsequent cycles reproduce the flow and pressure patterns with negligible variation. Hence, it was concluded that the 3 cycles were sufficient to resolve the simulation.

2.3 Timestep-Independence

A timestep independence study ensures that the results of the simulation are independent of the size of the timestep selected, avoiding aliasing and instability. Using the mean and maximum pressures at the foramen magnum, as well as the peak flowrate at the cervical spine extracted from the third cycle, Richardson extrapolation was applied to assess convergence between the three timesteps simulated.

Table D. Timestep sensitivity analysis for peak CSF flowrate and mean and peak pressure

	Order of convergence, p	**Percentage Error $\left(1-\frac{\phi_3}{\phi_{ext}}\right)\times 100$**	**Abs error $(\phi_{ext}-\phi_3)$**
Peak Flowrate [ml/min]			
Foramen Magnum	1.00	0.040	1.0E-04
Peak Pressure [Pa]			
C2	0.98	0.016	0.031
Mean Pressure [Pa]			
C2	3.16	0.006	0.006

The peak flowrate at the foramen magnum showed negligible deviation, with absolute errors in the order of $10^{-4}\ ml/min$ and relative errors well below 0.05%, as shown in Table D. Similarly, the mean and peak pressures at the cervical spine exhibited minimal absolute deviations and relative errors below 0.03%. These results demonstrate that the simulations are effectively timestep-independent at the chosen resolutions. Even for the relatively coarse T/20 timestep, the solution closely approximates the extrapolated values, confirming that the temporal resolution used is sufficient to capture the cyclic CSF dynamics accurately. This supports the decision to use a timestep of T/80 in the larger study.

REFERENCES

1. Rusbridge C, Stringer F, Knowler SP. Clinical Application of Diagnostic Imaging of Chiari-Like Malformation and Syringomyelia. Front Vet Sci. 2018 Nov 28;5. doi:10.3389/fvets.2018.00280

2. Jones R, Cirovic S, Rusbridge C. MRI-derived three-dimensional modelling reveals cervicothoracic subarachnoid space narrowing in syringomyelia-affected cavalier king charles spaniels. BMC Vet Res. 2026 Apr 1;22(1):306. doi:10.1186/s12917-026-05435-6

3. Fillingham P, Rane Levendovszky S, Andre J, Parsey C, Bindschadler M, Friedman S, et al. Patient-specific computational fluid dynamic simulation of cerebrospinal fluid flow in the intracranial space. Brain Res. 2022 Sep;1790:147962. doi:10.1016/j.brainres.2022.147962

4. Rich J, Hubler S, Vidondo B, Raillard M, Schweizer D. Influence of body weight, age, and sex on cerebrospinal fluid peak flow velocity in dogs without neurological disorders. J Vet Intern Med. 2024 May 25;38(3):1608–17. doi:10.1111/jvim.17073

5. Rasmussen CE, Vesterholm S, Ludvigsen TP, Häggström J, Pedersen HD, Moesgaard SG, et al. Holter monitoring in clinically healthy Cavalier King Charles Spaniels, Wire-haired Dachshunds, and Cairn Terriers. J Vet Intern Med. 2011 May;25(3):460–8.
6. Seymour RS, Angove SE, Snelling EP, Cassey P. Scaling of cerebral blood perfusion in primates and marsupials. Journal of Experimental Biology. 2015 Jan 1. doi:10.1242/jeb.124826
7. Novak G, Digel C, Burns B, James AE. Cerebrospinal fluid pressure measurements and radioisotope cisternography in dogs. Lab Anim. 1974 Jan 1;8(1):85–91. doi:10.1258/002367774780943779